

Quarterly Report for  
Contract DE-FG36-02ID14418  
**Stanford Geothermal Program**  
**July-September 2004**



## Table of Contents

<b>1. A FLOW-STRUCTURE MODEL FOR TWO-PHASE RELATIVE PERMEABILITIES IN FRACTURES</b>	<b>1</b>
1.1 INTRODUCTION	1
1.2 MODEL DESCRIPTION	2
1.3 EXPERIMENTS	7
1.4 RESULTS AND DISCUSSION	8
1.5 CONCLUSIONS	15
<b>2. EFFECT OF HETEROGENEITY ON CAPILLARY PRESSURE AND RELATIVE PERMEABILITY</b>	<b>17</b>
2.1 SUMMARY	17
2.2 THEORY	17
2.3 RESULTS	18
2.4 CONCLUSIONS	22
<b>3. FRACTURED ROCK RELATIVE PERMEABILITY</b>	<b>23</b>
3.1 BACKGROUND	23
3.2 EXPERIMENTAL METHODOLOGY	25
3.3 THEORETICAL BACKGROUND FOR ELECTRICAL RESISTIVITY	25
3.4 NITROGEN-WATER RELATIVE PERMEABILITY EXPERIMENTAL METHOD	26
3.5 NITROGEN-WATER RELATIVE PERMEABILITY RESULTS IN BEREA SANDSTONE	27
3.6 RESULTS OF ELECTRICAL RESISTIVITY MEASUREMENTS DURING FLOW	28
3.7 CONTINUING AND FUTURE WORK	29
<b>4. REFERENCES</b>	<b>31</b>

# **1. A FLOW-STRUCTURE MODEL FOR TWO-PHASE RELATIVE PERMEABILITIES IN FRACTURES**

This project is being conducted by Research Assistant Chih-Ying Chen and Prof. Roland Horne. The goal of this research was to model two-phase relative permeabilities in rough-walled fracture by using the proposed tortuous channel approach. In this study, we suggested an alternative approach to describe the two-phase relative permeability behavior in rough-walled fractures based on the two-phase flow structures. This approach lumps the microscale physical mechanism (viscous and capillary forces) into an apparent observable parameter, *channel tortuosity*, which was found to dominate the reduction of the relative permeabilities from the values that would be expected based on the X-curve. Three artificial fractures, smooth-walled, homogeneously rough-walled and randomly rough-walled fractures, were studied to represent distinct surface geometry and heterogeneity. The experimental results from these three fractures could be described successfully by the proposed model. Furthermore, we found that the magnitude of the channel tortuosity increases when the heterogeneity of the fracture surface increases. Although only three simplified fractures were studied and the relationship between the flow-based heterogeneity and the channel tortuosity is not fully developed yet, we were able to derive an empirical, tortuous channel model generalized from all channel tortuosities from these three fractures. This model can represent the current experimental data and as well as observations from earlier studies with good agreement.

## **1.1 INTRODUCTION**

Rock fractures or joints often form high-permeable flow pathways and therefore dominate single- or multiphase fluid transports in fractured porous media in the subsurface. Multiphase flows in fractured media are of great importance and engineering interest in geothermal development and environmental protection. In the last two decades, single-phase flow in fractures has been widely studied experimentally, numerically and theoretically. Several models have been proposed to describe the single-phase hydraulic properties in rough fractures (Witherspoon et al., 1980; Zimmerman and Bodvarsson, 1996; Meheust and Schmittbuhl, 2001; Lomize, 1951). However, limited studies have been done to determine the fundamentals of multiphase flow behavior in fractures, especially the effects of fracture geometry on relative permeabilities.

Chen et al. (2004a) suggested a phenomenological approach, the tortuous channel approach (TCA), to describe the air-water relative permeability behavior in a smooth-walled fracture. A method to evaluate the mutual tortuosities induced by the blocking phase, namely the *channel tortuosity*, was proposed from observations of the flow structure images. With verification from laboratory experiments and visualizations, it was concluded that in smooth-walled fractures the coefficients of channel tortuosity dominate the reduction of the relative permeability values from the X-curve (i.e. relative permeability equals saturation). The results also indicated that the X-curve relative permeability cannot be reached for two-phase flows in fractures even if their surfaces are smooth. Instead, an upper bound for the air-water relative permeability in fractures was proposed. Despite the successful representation of the experimental results in the smooth-walled fracture, the feasibility of using TCA to describe the relative permeabilities in rough fractures was not

studied – the rough-walled fracture represents a flow configuration much close to that expected in real rocks.

This research extended and modified the TCA to include rough-walled fractures. Existing and newly measured experimental data from two rough fractures with distinct surface roughness, randomly rough (RR) and homogeneously rough (HR), were used to evaluate and generalize this modified approach. Finally, a more general model deduced from these data was proposed to describe two-phase relative permeabilities in both smooth and rough fractures.

## **1.2 MODEL DESCRIPTION**

The diversity and variability of the geometry of a single, natural fracture and the complexity of the two-phase interaction and interference have made it difficult to reach a unique and accurate model to describe the two-phase flow behavior by means of the relative permeability concept. With the development of the visualization and surface measurement techniques, it has become possible to observe the multiphase flow behavior dynamically and to quantify the geometrical heterogeneity in fracture space. Nicholl et al. (2000) studied the effect of the immobile phase on the flowing-phase relative permeability in the saturated condition and developed a conceptual model for flowing-phase relative permeability by using the effective medium approach suggested by Zimmerman and Bodvarsson (1996). In the conceptual model of Nicholl et al. (2000), an in-place tortuosity induced by the immobile phase was used as a correction term to decrease the effective hydraulic gradient. The flowing-phase (water) relative permeability is then obtained as:

$$k_{rw} = S_w \tau_{ip} \underbrace{\left[ \frac{\langle b_f \rangle^2}{\langle b \rangle^2} \right] \left[ \left( 1 + \frac{9\sigma_b^2}{\langle b \rangle^2} \right)^{1/2} \left( 1 + \frac{9\sigma_{bf}^2}{\langle b_f \rangle^2} \right)^{-1/2} \right]}_A \quad (1.1)$$

where  $k_{rw}$  and  $S_w$  are the wetting-phase (water) relative permeability and saturation respectively,  $\langle b \rangle$  and  $\sigma_b^2$  are the mean and variance of the aperture field, the subscript (f) refers to parameters for the region occupied by the flowing phase, and  $\tau_{ip}$  (range from 0 to 1) is the in-place tortuosity. From their definition, the smaller the value of  $\tau_{ip}$ , the more tortuous the flowing phase structure behaves. Since their experiment was conducted in the saturated condition, nonwetting (air) phase remained entrapped. Nonwetting relative permeability was therefore always zero. From the experimental data, Nicholl et al. (2000) concluded that the in-place tortuosity is the dominant factor controlling the flowing phase relative permeability. However, the in-place tortuosity could not be measured in their study. Instead, in-place tortuosity was estimated independently by further simulating flow on the measured phase geometries under some simplified assumptions.

Chen et al. (2004a) conducted drainage (nonwetting phase displaces wetting phase) air-water cocurrent flow experiments in a smooth-walled fracture and defined a similar but measurable tortuosity coefficient for the channel flow regime, called channel tortuosity;  $\tau_c$ ,

and used this coefficient to characterize the morphology of flow structures. The definition of this apparent parameter is based on the area of the channel and the smallest bounding rectangle that covers the whole channel for a specific phase. By using digital video recording and image-processing techniques, thousands of continuous flow images were analyzed automatically, and different flow structures were recognized and separated. It was found that the channel flow was the major flow structure spanning most of the water saturation ( $S_w$ ) range, except for extremely small or large values of  $S_w$ . The channel area,  $A_c$ , length and width of the smallest bounding box,  $L_x$  and  $L_y$ , were computed for channels of each phase. The channel tortuosities for gas and water were then defined as:

$$\tau_{c,g} = \left(\frac{L_x L_y}{A_c}\right)_g \quad \text{and} \quad \tau_{c,w} = \left(\frac{L_x L_y}{A_c}\right)_w \quad (1.2)$$

where the subscripts ( $_g$ ) and ( $_w$ ) denote the gas and water phases respectively.

The detailed methodology and an illustration of the computation of  $\tau_c$  can be found in Chen et al. (2004a). Similar to the definition in porous media, the coefficient  $\tau_c$  for each phase varies from 1 to infinity, with the two end cases representing respectively a homogeneous straight channel (no dispersed phase) and an extremely tortuous channel for each phase. This coefficient is related to the interfacial area and, consequently, allows quantification of the shear stress at the interface between the two fluids. From the experimental data, Chen et al. (2004a) found that the coefficients of channel tortuosity dominate the reduction of relative permeability in comparison to the X-curve, and that the following relative permeability relationship could replicate the experimental data with good accuracy:

$$k_{rw} = \frac{S_w}{\tau_{c,w}} \quad (1.3)$$

$$k_{rg} = \frac{S_g}{\tau_{c,g}} \quad (1.4)$$

It is worth noting that because of their different definitions of the tortuosity, the  $\tau_{cw}$  in Equation (1.3) and  $\tau_{ip}$  in Equation (1.1) should be close to reciprocal. Therefore, for smooth-walled fractures ( $\langle\langle b \rangle\rangle = \langle b_f \rangle$  and  $\sigma_b^2 = \sigma_{bf}^2$ ), and Equation (1.1) can be simplified to Equation (1.3).

For the drainage relative permeabilities in rough-walled fractures, a major factor that was not considered in Equations (1.3) and (1.4) was the residual water, which was observed to be negligible in the smooth-walled case. The significant capillary force due to local aperture field variation can entrap considerable amounts of water phase, and some of it will contribute to the residual water saturation ( $S_{wr}$ ) ultimately. To this end, a more rigorous approach by separating different phase structures was developed. Figure 1.1 illustrates the

principle and concepts of this rough-walled tortuous channel approach. The two-phase flow structures were separated into three major parts, namely the flowing channels, the entrapped phases and the water film flowing along the fracture surfaces. During the steady-state drainage process, the first two parts were fully or partially included in the channel tortuosity terms, except for the considerable immobile and residual water phase. In analogy to earlier studies of relative permeability modeling in porous media (Brooks and Corey, 1966; van Genuchten, 1980), the immobile and residual phases were taken into account by normalizing the water saturation. For the drainage process, the normalized water saturation is:

$$S_w^* = \frac{S_w - S_{wr}}{1 - S_{wr}} \quad (1.5)$$

where subscript ( $r$ ) refers to residual saturation.

Regarding the water film flow along the fracture surfaces, an extended two-dimensional viscous coupling model was used to evaluate the effect of film thickness on relative permeabilities. The one-dimensional viscous coupling model was obtained by integrating Stoke's equations under parallel-plate assumption. The one-dimensional model was then defines as:

$$k_{rw} = \frac{S_w^2}{2} (3 - S_w) \quad (1.6)$$

$$k_{rg} = (1 - S_w)^3 + \frac{3}{2} \mu_r S_w (1 - S_w)(2 - S_w) \quad (1.7)$$

where  $\mu_r = \mu_g/\mu_w$  is the viscosity ratio.

Since the one-dimensional viscous coupling model has poor representation of the real two-phase flow behaviors in fractures, the simplified but more practical geometrical consideration of the drainage process in an ideal fracture space is shown in Figure 1.2. The gas channel was initially assumed to be in a round-ended rectangular column with constant height,  $H_w$ , which is close to but always smaller than the fracture aperture,  $b$ . The relative permeability was computed by using either the superposition or integration of the one-dimensional solution in each vertical slice as shown in Figure 1.2. After the gas channel reaches the fracture boundaries (Stage 2), the gas phase starts to expend vertically and the corresponding relative permeability approximately follows one-dimensional viscous coupling in Stage 3. By setting different values of the water film ratio,  $H_w/b$ , and assuming the fracture width was much larger than its aperture, the effect of water film thickness on air-water relative permeabilities is shown in Figure 1.3. The water film ratio affects the relative permeabilities almost linearly because the scale of the fracture aperture is relatively small. In addition, the effect on gas-phase relative permeabilities is stronger than on the water phase. Consequently, film flow correctors,  $F_{mw}$  and  $F_{mg}$ , were suggested as

corrections to the relative permeabilities to account for the water film flow. Combining all factors in Figure 1.1, the modified TCA for describing the relative permeabilities of the rough fractures can be written in the following form:

$$k_{rw} = \frac{S_w^*}{\tau_{c,w}} F_{mw} \quad (1.8)$$

$$k_{rg} = \frac{S_g}{\tau_{c,g}} F_{mg} \quad (1.9)$$

Comparing Equation (1.8) to Equation (1.1) and examining the definition of the channel tortuosities, we can see that part A in Equation (1.1) has inherently contributed to the coefficients of  $\tau_{c,w}$ , and  $S_w^*$ .

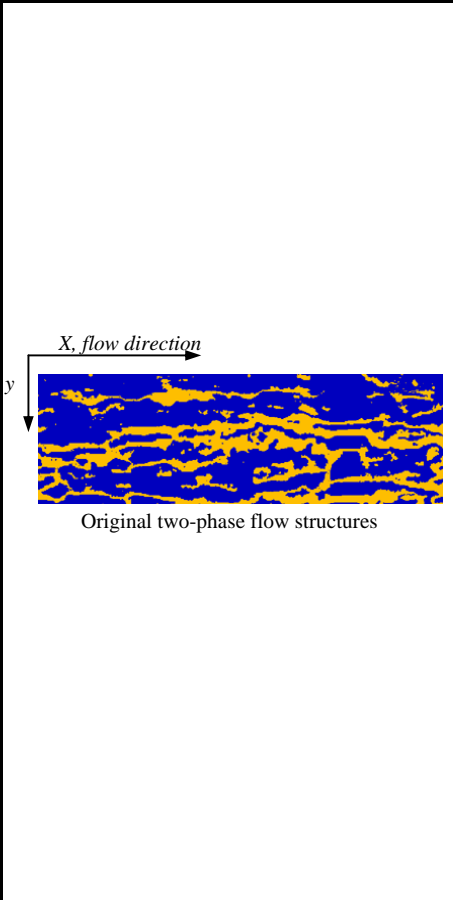
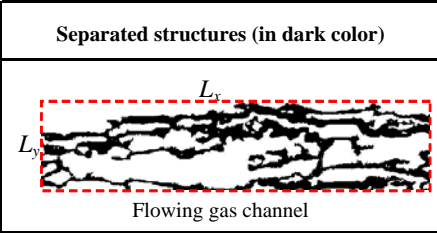
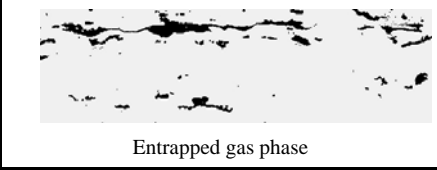
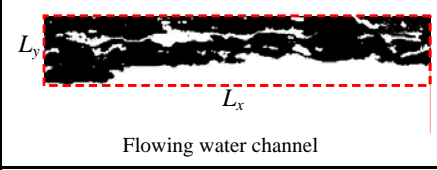
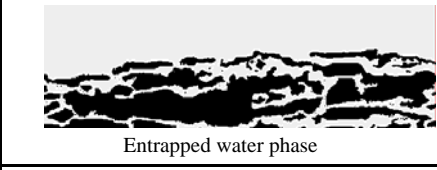
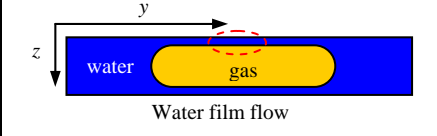
	Separated structures (in dark color)	Major impact	Included terms
 <p>Original two-phase flow structures</p>	 <p>Flowing gas channel</p>	<ul style="list-style-type: none"> <li>Gas rates</li> <li>Gas tortuosity</li> </ul>	$\tau_{c,g}$
	 <p>Entrapped gas phase</p>	<ul style="list-style-type: none"> <li>Water tortuosity</li> </ul>	$\tau_{c,w}$
	 <p>Flowing water channel</p>	<ul style="list-style-type: none"> <li>Water rates</li> <li>Water tortuosity</li> </ul>	$\tau_{c,w}$
	 <p>Entrapped water phase</p>	<ul style="list-style-type: none"> <li>Gas tortuosity</li> <li>Immobile water saturation</li> </ul>	$\tau_{c,g}$ $S_{wr}$
	 <p>Water film flow</p>	<ul style="list-style-type: none"> <li>Gas rates</li> <li>Water rates</li> </ul>	$F_m$

Figure 1.1: Illustration of separating the two-phase flow structures and the major impact parameters in each separated structure considered in the rough-walled TCA for drainage process

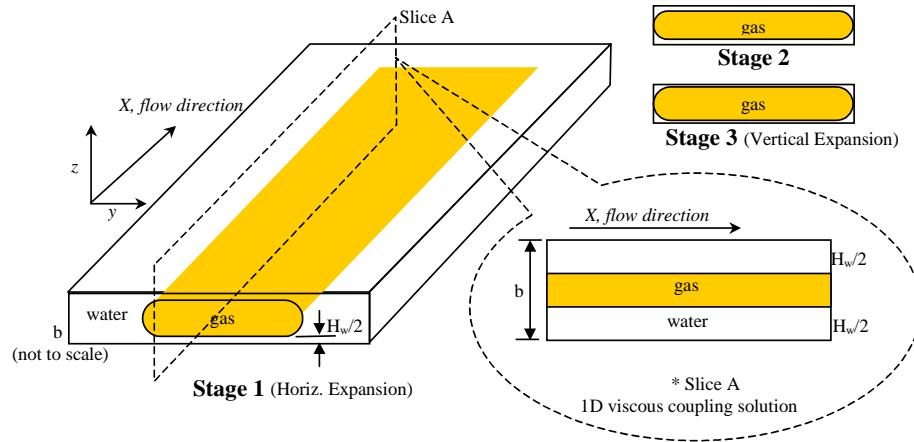


Figure 1.2: A simple superposition method for integrating one-dimensional viscous coupling model to two-dimensional viscous coupling model. The water film thickness,  $H_w$ , was assumed being constant during stage 1 and 2. After Stage 2, the  $H_w$  starts decreasing and the corresponding relative permeabilities approximately follows one-dimensional viscous coupling. ( $b$  and  $H_w$  are not to scale)

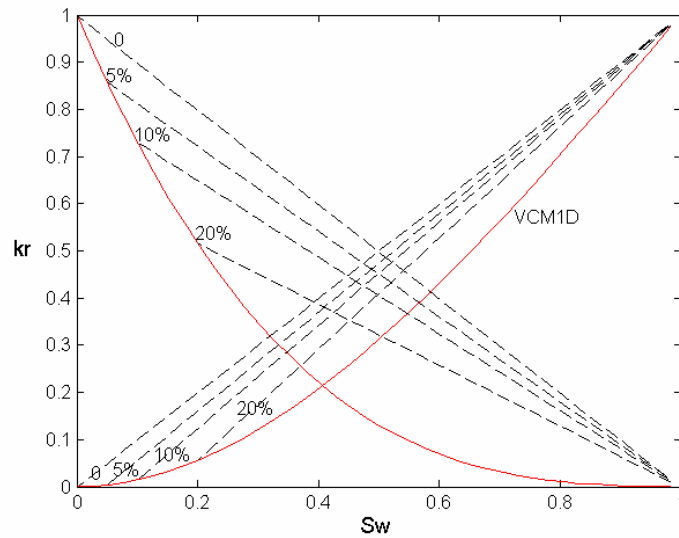


Figure 1.3: Effect of water film thickness on air-water relative permeabilities. VCM1D is the one-dimensional viscous coupling model. The percentage means the water film ratio ( $H_w/b$ ).

Generally, the water film in partially saturated rock surfaces is attributed to adsorptive forces on flat surfaces of minerals or by capillary effects within the surface roughness. The metric potential is the major parameter that controls the thickness of the film. By considering the fracture-matrix interaction in fractured porous media, Tokunaga and Wan (1997) measured average surface film thickness ranging from 2 to 70  $\mu\text{m}$ . However, for a single fracture with an impermeable matrix as in our cases, earlier studies indicated that the

water film ratio was less than 1% (Romm, 1966; Pan et al., 1996) for smooth-walled fractures. However this ratio may increase for the rough-walled fractures since surface roughness and pits on the surface increase capillary and absorption forces. To the best of our knowledge, no practical methods exist to estimate the  $H_w$  in accordance with different surface geometry for a single fracture with impermeable surfaces. Judging from the study by Romm (1966) and the corresponding result in Figure 1.3, the water film ratio should be small and  $F_m$  should be close to 1, which means that the film effect on the relative permeabilities may be insignificant. Following this result, Equations (1.8) and (1.9) can be further simplified to:

$$k_{rw} = \frac{S_w^*}{\tau_{c,w}} \quad (1.10)$$

$$k_{rg} = \frac{S_g}{\tau_{c,g}} \quad (1.11)$$

In these simple equations, only two measurable parameters are needed. The residual saturation is readily obtained in the laboratory; however, the channel tortuosity has to be obtained by the aid of tomography or visualization techniques during two-phase flow experiments, unless some correlation between channel tortuosities and fracture geometry can be built to predict the channel tortuosity. To this end, several experiments were conducted to explore this issue and verify the model.

### **1.3 EXPERIMENTS**

The fractures for the experiments were made by transparent silica glass with dimensions around 30cm (L) x 10cm (W). Two fractures with distinct surface roughness, randomly rough (RR) and homogeneously rough (HR) fractures, were used in the steady-state air-water cocurrent drainage experiments to represent two distinct surface geometries and heterogeneities. The experiment of the RR case was conducted during this study while the data from the HR case were provided by an earlier experiment (Chen et al. 2004b). Details of the experimental apparatus and procedures can be found in Chen et al. (2004a). The three-dimensional profile of the RR fracture and the two-dimensional surface pattern of the HR fracture are shown in Figure 1.4. The RR fracture has a hydraulic aperture of around 240  $\mu\text{m}$  ( $\sim 4800$  darcy in permeability). The three-dimensional surface profile was measured by Leitz PMM 12106 CMM Stylus Machine (20 microns resolution,  $\sim 2$  microns precision). The HR fracture has repeatable wedge-shaped pattern with hydraulic aperture of around 145  $\mu\text{m}$  ( $\sim 1750$  darcy in permeability).

Initially, the fractures were fully saturated with deionized water. The drainage process was controlled by adjusting water and gas injection rates to decrease the water saturation. First, the water rate was kept constant while increasing gas rate to decrease the water saturation through the fracture until the water saturation was no longer sensitive to the increase of the gas rates. Then, the water rate was decreased further and the previous procedure was

repeated. To avoid the dissolution of the gas phase and evaporation of the water phase, the water was equilibrated with air and the nitrogen gas was saturated with water-vapor. During each designated input rate of gas and water, the data were acquired when a stable or repeatable flow structure had been reached. After finishing one run (one pair of prescribed water and gas rates), the flow structures were destroyed by rapidly flushing water through the fractures, and then another run was commenced.

According to air-water experiments reported by earlier studies (Persoff and Pruess, 1995; Diomampo, 2001; Chen et al. 2004a), the fracture flow experiments are unsteady by nature. While input rates of water and gas were fixed, considerable pressure fluctuations accompanied by corresponding saturation changes occurred, which made flow rates through the fractures vary. A traditional time-average data processing was deemed to be infeasible and unrepresentative since every datum fluctuation may indicate a corresponding fluctuation of flow structure and saturation. To overcome these issues, all instantaneous data were acquired in a period less than or equal to one second. The high-speed data acquisition system gathered instantaneous pressure and flow rate, while instantaneous gathering of saturation and flow structure data was accomplished by the use of the digital video camcorder and automatic image processing techniques.

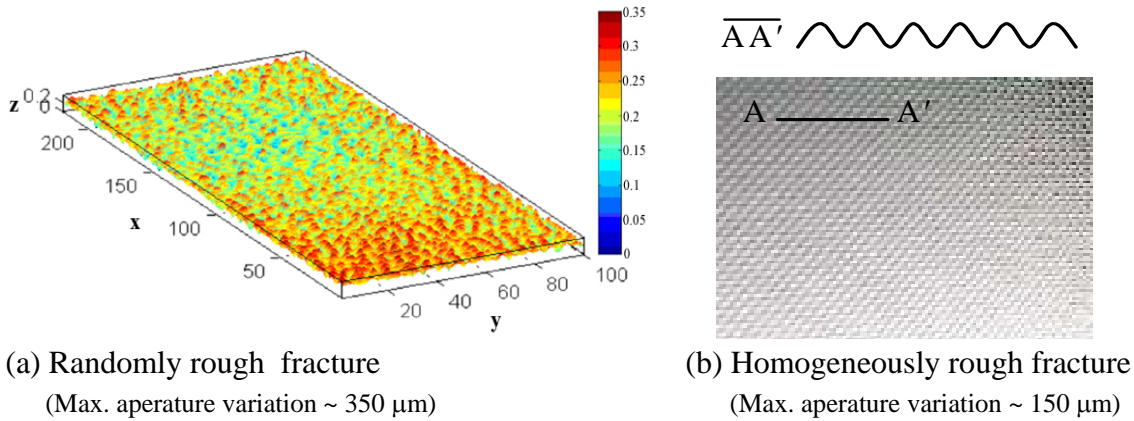


Figure 1.4: Surface profile of the rough-walled fractures: (a) three-dimensional profile of the RR fracture; (b) two-dimensional surface pattern of the HR fracture.

## 1.4 RESULTS AND DISCUSSION

Around 3000 data points were obtained in each experiment within a period of 1 second. The information of pressure, rates and saturation were then used to compute relative permeabilities using generalized two-phase Darcy equations. These experimental results served as the reference relative permeabilities to validate the suggested model (Equations (1.10) and (1.11)). Continuous flow images from these experiments were analyzed. Phase channels were recognized, and the  $\tau_{c,w}$  and  $\tau_{c,g}$  values were then computed. Figure 1.5 shows several representative images extracted from these two experiments as well as the smooth-walled images replicated from Chen et al. (2004a). Snapshots in each row in Figure 1.5 have similar water saturation but are from different type of fractures. Clearly, the channel tortuosity increases when the heterogeneity of the fracture surface increases.

The phase channels in RR fracture are always the most tortuous among these three cases. In general, for a specific fracture, the channel tortuosity of one phase has a countertrend to the saturation of that phase. In other words, the water (gas) channel tortuosity increases when the water (gas) saturation decreases. With increasing surface heterogeneity, the nested behavior of flow structures was increasingly apparent. Even though the flow structures were destroyed before changing the input rates, the gas phase had some stationary preferential pathways in the rough fractures, particularly in the RR fracture. When the gas saturation increased further, the gas channels expanded from these base pathways or branched from them. This behavior may demonstrate the likely flow structure evolution in natural fractures.

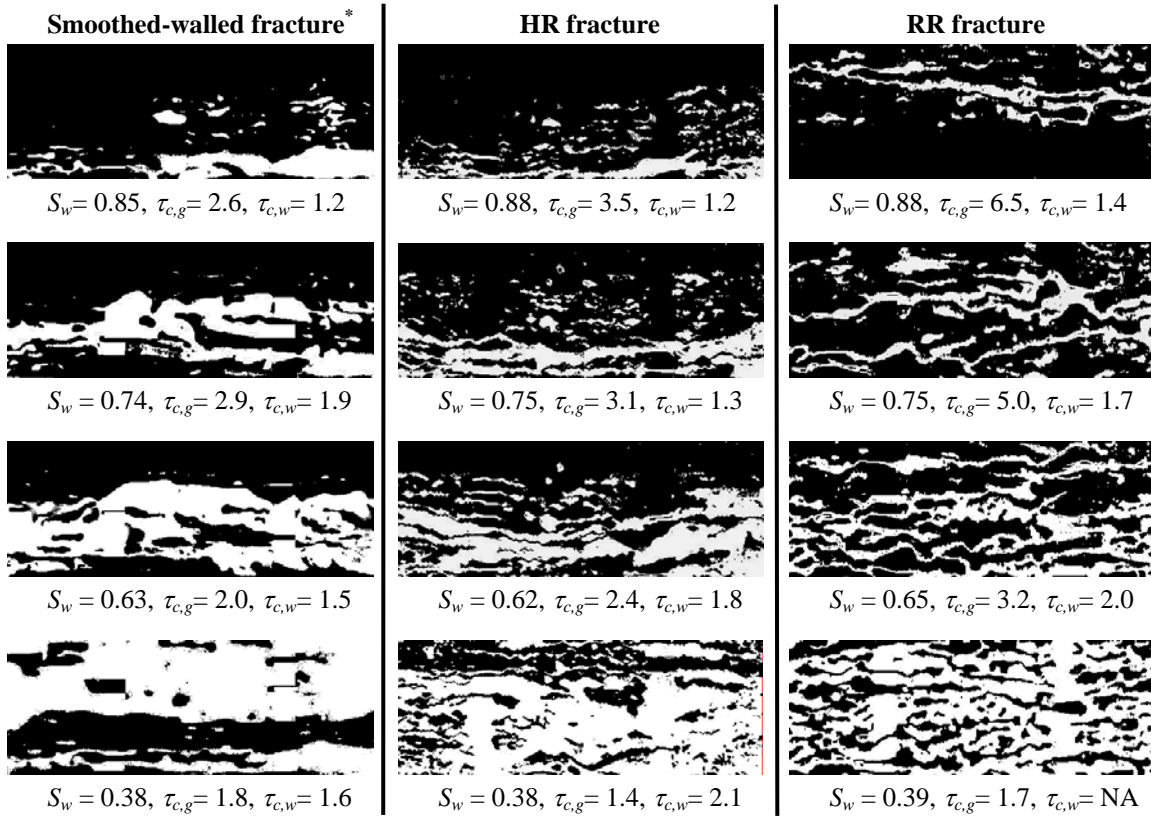


Figure 1.5: Representative images extracted from the image-processing program of channel recognition for the smooth and rough fractures and corresponding channel tortuosities evaluated (Gas phase is white and water is black. \*Smooth-walled images are from Chen et al., 2004a)

After analyzing thousands of images, the channel tortuosities of each phase were evaluated, and then the relative permeabilities were computed using the proposed TCA in Equations (1.10) and (1.11). Figures 1.6 and 1.7 compare these results to the reference experimental relative permeabilities from the generalized Darcy equations for the RR and FR fractures respectively. Due to the unstable nature of the flow, the experimental relative permeabilities are scattered. For the RR fracture, the result from TCA fits the experimental result with good accuracy. The gas-phase relative permeabilities seem to be overestimated

slightly. Close agreement was also obtained in the HR fracture case. However, the gas-phase values from TCA were larger than the experimental result. The overestimation in gas-phase relative permeability may be attributed to the water film flow effect as demonstrated in the previous section (but neglected in the current study), or the experimental and image processing errors. The major source of the image processing errors was from the recognition of the channel connectivity, particularly for the rough-walled fractures. Because of the local aperture variation, some phase channels were connected via thin threads that were too narrow to be recognized in the images in a few cases. This led to the less accurate calculation of tortuosity.

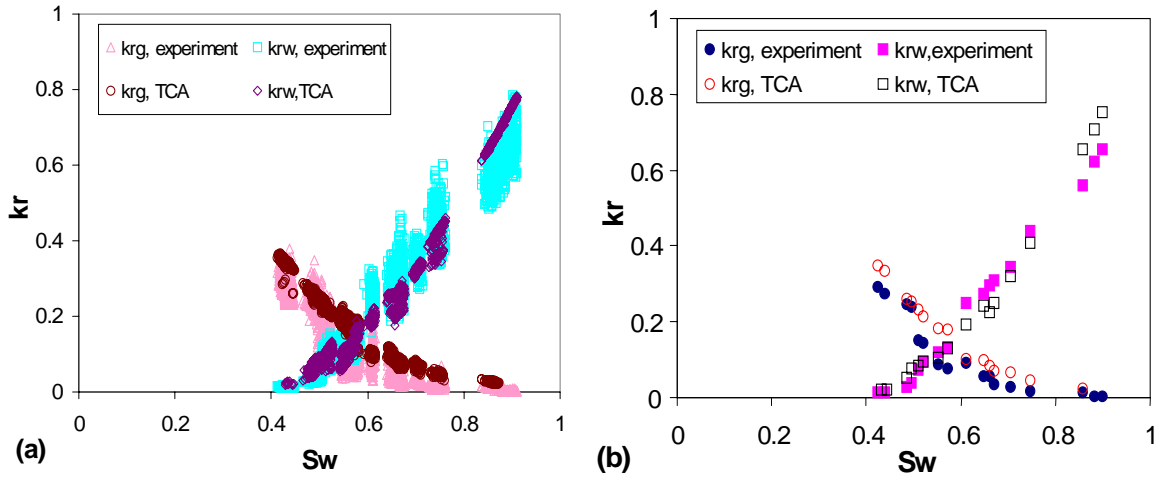


Figure 1.6: Relative permeabilities from tortuous-channel approach and its comparison with the experimental result for the RR fracture: (a) all data points (~3000 points), (b) averages of each runs in (a).

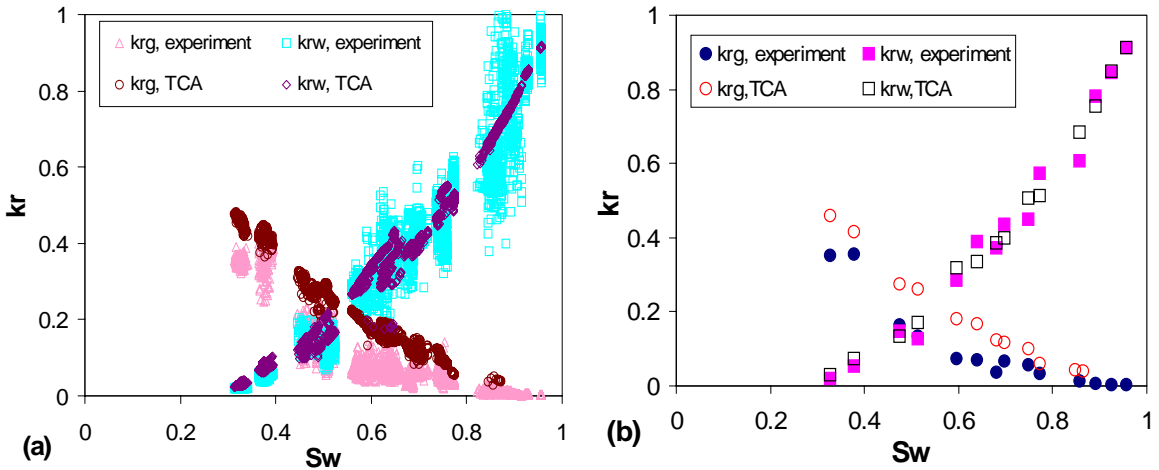


Figure 1.7: Relative permeabilities from tortuous-channel approach and its comparison with the experimental result for the HR fracture: (a) all data points (~3000 points), (b) averages of each runs in (a).

The evolution of phase channels shown in Figure 1.5 may reveal the correlation between the channel tortuosity and the surface geometry and heterogeneity of fractures. Earlier studies also suggested that relative permeabilities in fractures are sensitive to the nature and range of spatial correlation between apertures (Pruess and Tsang, 1990). Combining current results with the smooth-walled results from Chen et al. (2004a), Figure 1.8a shows the reciprocal of water-phase tortuosity versus water saturation for all of the fractures studied. A straight channel has a value of reciprocal of tortuosity equal to 1. As can be seen in this figure, acceptable linear trends can be found in these three cases, while their slopes increase when the heterogeneity of the fracture surfaces increases. Interestingly, these data seem to collapse to a single linear trendline when plotted in normalized water saturation as shown in Figure 1.8b. On the other hand, the gas channel tortuosities show similar trends in the smooth and the HR fractures while the RR fracture results demonstrate a slightly more tortuous trend as shown in Figure 1.9. However, most of the deviated points in Figure 1.9 were close to the end point of the gas saturation, which has less a significant inference on the Equations (1.10) and (1.11). All of these gas-phase tortuosities can be expressed approximately in a second-order relationship with respect to gas saturation.

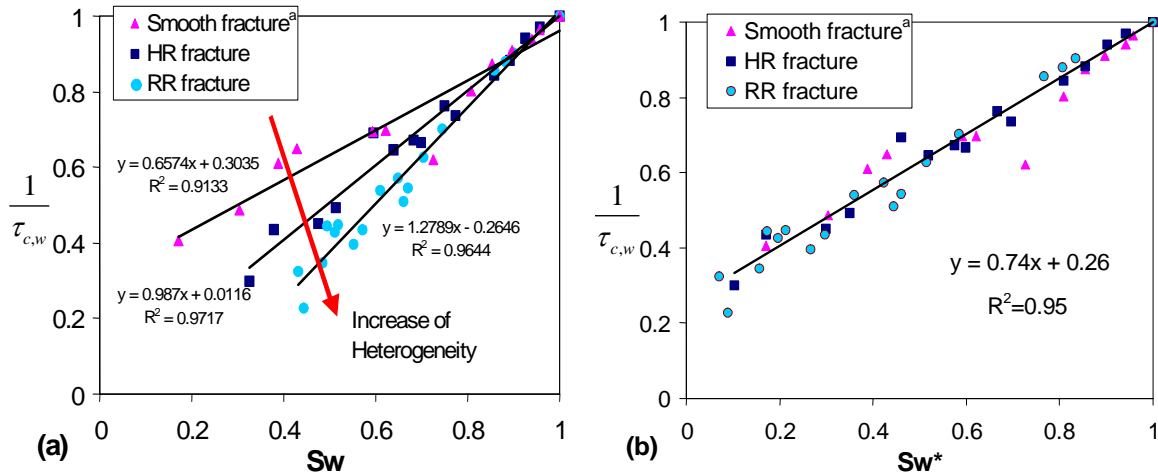


Figure 1.8: Reciprocal of average water channel tortuosity versus (a) water saturation and (b) normalized water saturation for smooth and rough fractures. ( <sup>a</sup> : from Chen et al., 2004a)

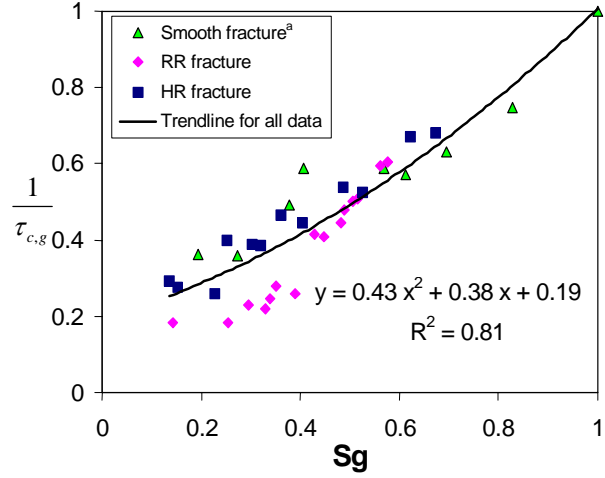


Figure 1.9: Reciprocal of average gas channel tortuosity versus gas saturation for smooth and rough fractures. (<sup>a</sup>: from Chen et al., 2004a)

Generalizing from these three specific types of fractures, preliminary and empirical correlation equations between the channel tortuosity and saturation can be obtained as shown in Figures 1.8b and 1.9. Substituting these equations into Equations (1.10) and (1.11), the tortuous channel model (TCM) for the three fractures we studied is then obtained as:

$$k_{rw} = 0.74S_w^{*2} + 0.26S_w^* \quad (1.12)$$

$$k_{rg} = 0.43S_g^3 + 0.38S_g^2 + 0.19S_g \quad (1.13)$$

Fitting this model to the experimental results is shown in Figure 1.10. Close agreement was obtained between this tortuous channel model and the experimental measurements. Using measured values of residual water saturation  $S_{wr}$  from the experiments of the rough fractures, this model can describe the water-phase relative permeabilities with good accuracy, accounting for the residual phase. The gas-phase curve generalized from all gas-phase tortuosities seems to overestimate  $k_{rg}$  slightly compared to the experimental result; nevertheless the model curve can still capture the trend of the experimental data.

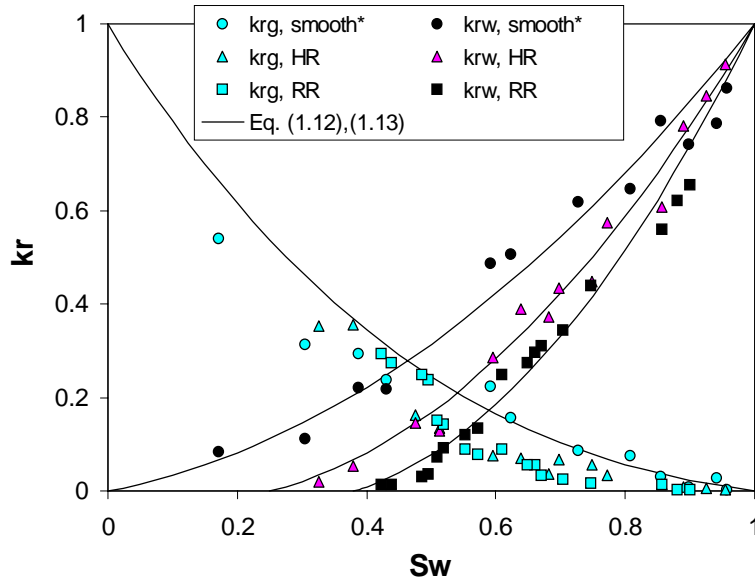


Figure 1.10: Comparison of the experimental relative permeabilities with tortuous-channel model using Equations (1.12) and (1.13) for the smooth-walled, HR and RR fractures. The  $S_{wr}$  for HR and RR fractures is 0.25 and 0.39 respectively determined from the experiments. (\*: from Chen et al., 2004a)

Nicholl and Glass (1994) conducted experiments to measure flowing-phase (water phase) relative permeabilities in the presence of entrapped gas phase in a homogeneous, isotropic fracture. The corresponding in-place tortuosities were inferred from simulated flow rates using measured phase geometries (Nicholl et al., 2000). Although their experiments were conducted in saturated condition (water was the only flowing phase) and the final residual water saturation was not reported, Equation (1.10) still shows an acceptable fit to their flowing relative permeabilities by using their simulated tortuosities and setting a reasonable value for  $S_{wr}$  (0.36), as illustrated in Figure 1.11. In addition, most of the simulated tortuosities fall on the linear trendline suggested in this study (Figure 1.12). Pruess and Tsang (1990) predicted fracture relative permeabilities from numerical simulation of conceptual and heterogeneous fracture geometries. The phase occupancy and permeability were derived by assuming a parallel-plate model for small subregions in the fracture plane. Although only qualitative applications were suggested and the nonwetting phase relative permeabilities were deemed to be less physical in their simulated results, the wetting-phase relative permeabilities did follow a conventional pattern. As shown in Figure 1.13, these numerical results can be interpreted by the proposed tortuous channel model by setting a reasonable value for  $S_{wr}$ .

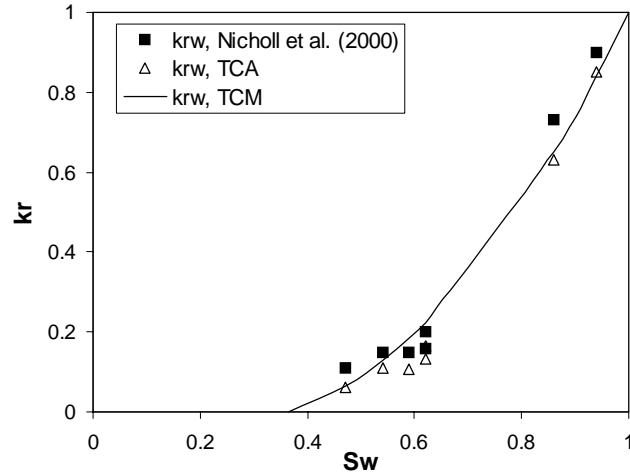


Figure 1.11: Using proposed TCA and TCM to interpret flowing-phase relative permeabilities from Nicholl et al. (2000) by setting  $S_{wr} = 0.36$ .

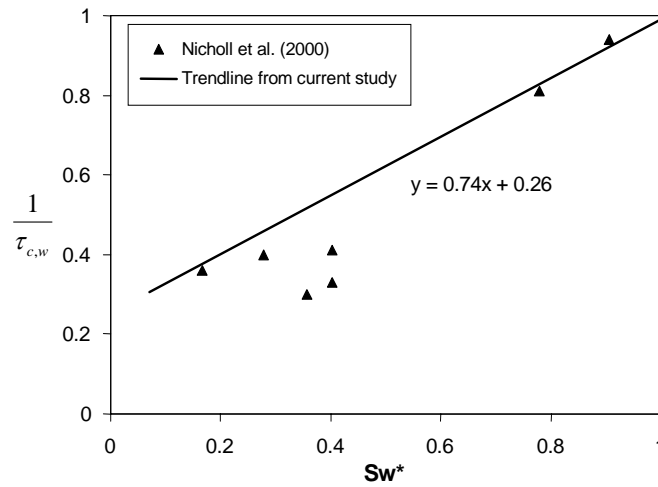


Figure 1.12: Plot of reciprocal of in-place tortuosities from Nicholl et al. (2000) versus normalized water saturation by setting  $S_{wr} = 0.36$ .

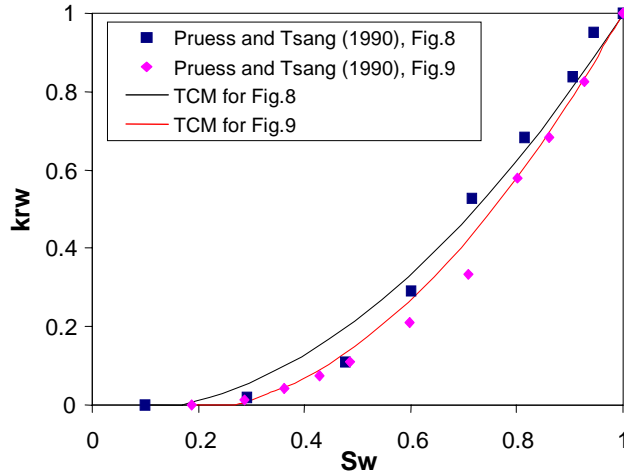


Figure 1.13: Using proposed tortuous channel model (Equations (1.12) and (1.13)) to interpret the water-phase relative permeabilities from earlier numerical study done by Pruess and Tsang (1990). ( $S_{wr}$  was set to be 0.27 and 0.17 respectively)

## **1.5 CONCLUSIONS**

This study has demonstrated the possibility of using a flow-structure model to predict the corresponding relative permeabilities in rough-walled fractures. The proposed approach can represent the experimental data from current and earlier studies with good agreement. By studying three fractures with different surface roughness, we found that the magnitude of the flow channel tortuosity increases when the heterogeneity of fracture surface increases. Generalizing from all the channel tortuosities measured in these three fractures, we suggested an empirical, tortuous channel model. Although some successful descriptions of relative permeabilities in rough-walled fractures using the proposed tortuous channel approach and model were achieved, it is very important to emphasize the limitations. At this moment, the method of evaluating the coefficient of tortuosity and the feasibility of using the tortuous-channel approach were only validated in specific artificial fractures made of silica glass. To account for the complex connectivity and flow structures in full-scale naturally-fractured media, the algorithm to evaluate  $\tau_c$  and the methodology to characterize the flow-based heterogeneity may have to be developed further. Characterizing the flow-based heterogeneity of the fractures is believed to be the major challenge of the future application. The tortuous-channel model (Equations (1.12) and (1.13)) was developed from current results empirically. The characteristics of heterogeneity in natural fractures are certainly much more complex and variable. Therefore more studies of the relationship between tortuosity and fracture geometry may be needed to gain rigorous models for predicting fracture relative permeabilities accurately. If such work can be achieved, perhaps the relative permeabilities of natural fractures can be predicted simply by measuring  $S_{wr}$  and the geometry of the fracture surface or by using tomographic technology to determine channel tortuosity.



## **2. EFFECT OF HETEROGENEITY ON CAPILLARY PRESSURE AND RELATIVE PERMEABILITY**

This research project is being conducted by Senior Research Engineer Kewen Li and Prof. Roland Horne. The objective of this project is to study the effect of heterogeneity and other parameters on the capillary pressure and relative permeability of geothermal rocks.

### **2.1 SUMMARY**

Using the universal capillary pressure model developed recently, the effects of heterogeneity, entry capillary pressure, and maximum capillary pressure on the shape of capillary pressure curves were studied. It was found that the shape of capillary pressure curves is influenced by not only the heterogeneity but also the entry and maximum capillary pressure in the cases where  $D_f$  is greater than 3.

### **2.2 THEORY**

The capillary pressure model used in this study is expressed as follows:

$$P_c = p_{\max} (1 - bS_w^*)^{-\frac{1}{\lambda}} \quad (2.1)$$

where  $p_{\max}$  is the capillary pressure at the residual wetting phase saturation in the drainage case or the maximum capillary pressure.  $b$  is a constant and expressed as follows:

$$b = 1 - \left( \frac{P_e}{P_{\max}} \right)^{-\lambda} \quad (2.2)$$

where  $p_e$  is the entry capillary pressure in the drainage case.  $\lambda = 3 - D_f$ .  $D_f$  is the fractal dimension, which is a representation of the heterogeneity of rock. The greater the fractal dimension, the greater the heterogeneity. Note that the pore size distribution index  $\lambda$  in the Brooks-Corey capillary pressure model is also a representation of the heterogeneity. The greater the pore size distribution index, the less the heterogeneity of a porous medium.

In Eq. 2.1,  $S_w^*$  is the normalized wetting phase saturation, which could be expressed as follows in the drainage case:

$$S_w^* = \frac{S_w - S_{wr}}{1 - S_{wr}} \quad (2.3)$$

where  $S_{wr}$  is the residual saturation of the wetting phase.

The new relative permeability model derived from the generalized capillary pressure model (Eq. 2.1) using the Burdine approach is expressed as follows:

$$k_{rw} = \frac{(S_w^*)^2 [(1 - bS_w^*)^m - 1]}{(1 - b)^m - 1} \quad (2.4)$$

$$k_{rnw} = \frac{(1 - S_w^*)^2 [(1 - b)^m - (1 - bS_w^*)^m]}{(1 - b)^m - 1} \quad (2.5)$$

where  $k_{rw}$  and  $k_{rnw}$  are the relative permeability of the wetting phase and the nonwetting phase.

The new relative permeability model derived from the generalized capillary pressure model using the Purcell approach is expressed as follows:

$$k_{rw} = \frac{[(1 - bS_w^*)^m - 1]}{(1 - b)^m - 1} \quad (2.6)$$

$$k_{rnw} = \frac{[(1 - b)^m - (1 - bS_w^*)^m]}{(1 - b)^m - 1} \quad (2.7)$$

where  $m$  is defined as follows:

$$m = \frac{2 + \lambda}{\lambda} = \frac{5 - D_f}{3 - D_f} \quad (2.8)$$

Basically the difference between the Burdine and the Purcell approaches is the consideration of the effect of tortuosity which is included in the Burdine approach but not included in the Purcell approach.

## **2.3 RESULTS**

The theoretical capillary pressure data were calculated using Eq. 2.1 with different values of fractal dimension and the results are shown in Fig. 2.1. The values of fractal dimension used in the calculation were 2.0, 2.5, 2.9, 3.3 and 3.8. The values of maximum capillary pressure and entry capillary pressure were 100 atm and 0.4 atm respectively in Fig. 2.1. The residual wetting-phase saturation was 20%. In the case where  $D_f < 3.0$ , the capillary pressure curve is convex to the axis of the wetting-phase saturation and looks like a common capillary pressure curve (for example, the capillary pressure curve of Berea sandstone). This type of capillary pressure curve can usually be represented mathematically by the Brooks-Corey model in cases in which  $p_e/p_{max}$  is negligible. In the case where  $D_f > 3.0$ , the capillary pressure curve is concave to the axis of the wetting-phase saturation (see Fig. 2.1). The capillary pressure curves of The Geysers rock have such a feature (Li and Horne, 2003). One can see from Fig. 2.1 that not only the magnitude of

capillary pressure but also the shape of the curves is influenced significantly by the heterogeneity of rock, represented by the fractal dimension.

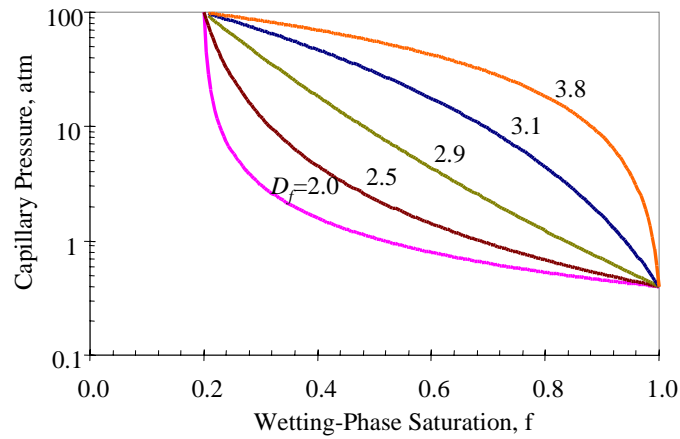


Figure 2.1: Typical capillary pressure curves calculated using the universal model with different values of fractal dimension.

Fig. 2.2 shows the normalized capillary pressure curves using the data shown in Fig. 2.1. In the case in which  $D_f$  is equal to 2.0, the relationship between capillary pressure and the normalized wetting phase saturation is linear. However the normalized capillary pressure curves with  $D_f$  other than 2.0 are not straight lines.

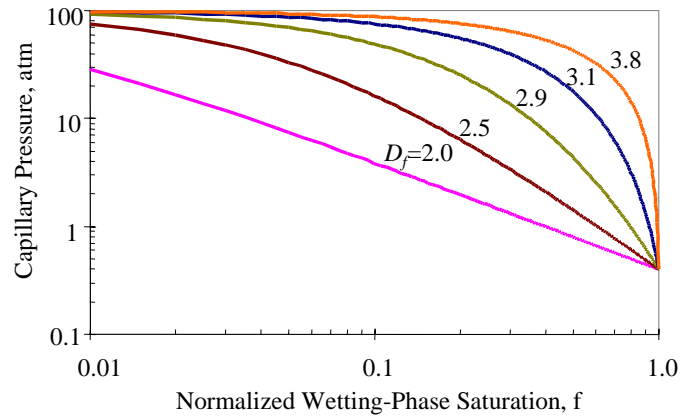


Figure 2.2: Normalized capillary pressure curves calculated using the universal model with different values of fractal dimension.

The effect of the entry capillary pressure ( $p_e$ ) on the shape of capillary pressure curves is shown in Fig. 2.3.  $D_f$  is equal to 2.5 and  $p_{max} = 100$  atm in Fig. 2.3. One can see that the relationship between capillary pressure and the normalized wetting phase saturation is linear if  $p_e$  is less than a specific value. Otherwise, it is not linear. When  $D_f$  increases from 2.5 to 2.9, the normalized capillary pressure curves calculated using Eq. 9 are plotted in Fig. 2.4. In this case, all the curves are highly nonlinear.

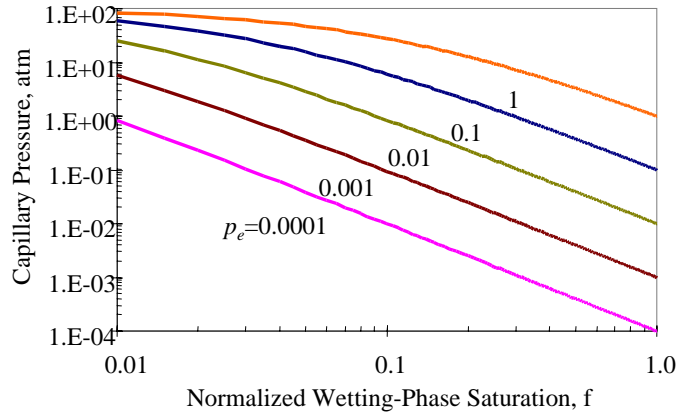


Figure 2.3: Normalized capillary pressure curves calculated with different values of entry capillary pressure ( $D_f=2.5$ ).

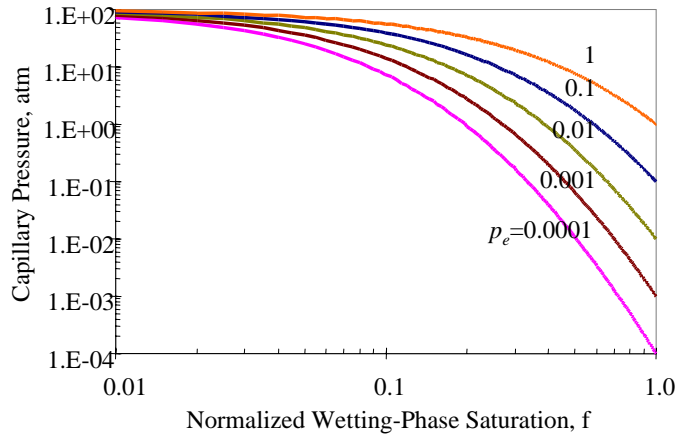


Figure 2.4: Normalized capillary pressure curves calculated with different values of entry capillary pressure ( $D_f=2.9$ ).

Fig. 2.5 shows the effect of  $p_{max}$  on the capillary pressure curves.  $D_f$  is equal to 2.5 and  $p_e = 0.4$  atm in Fig. 2.5. The value of  $p_{max}$  ranges from 10 to  $10^5$  atm. The normalized capillary pressure curves are linear if  $p_{max}$  is greater than a specific value. When  $D_f$  increases from 2.5 to 2.9, the normalized capillary pressure curves calculated using Eq. 9 are plotted in Fig. 2.6. With  $D_f=2.9$ , all the curves become nonlinear.

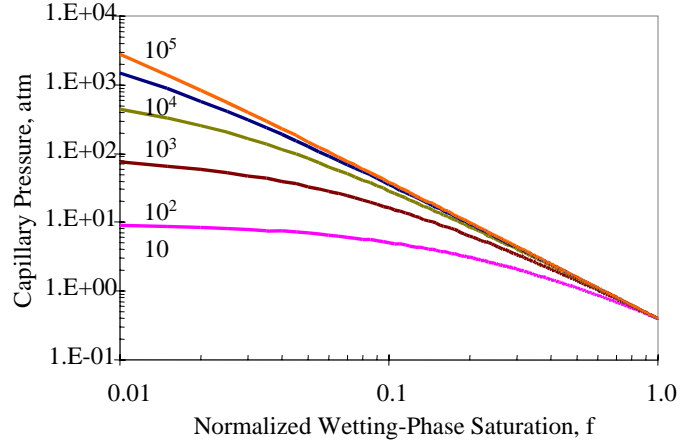


Figure 2.5: Normalized capillary pressure curves calculated with different values of  $p_{max}$  ( $D_f=2.5$ ).

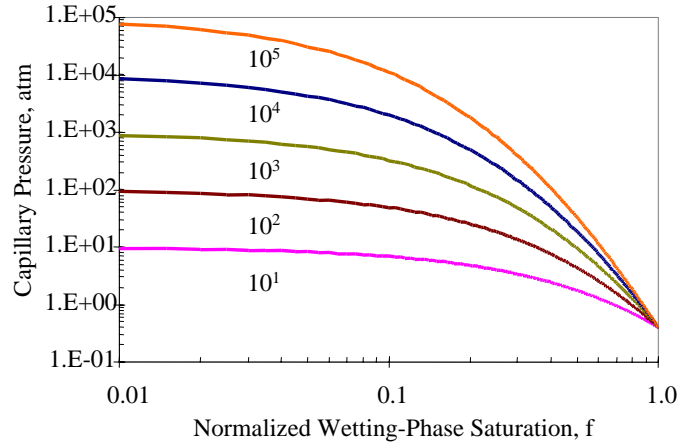


Figure 2.6: Normalized capillary pressure curves calculated with different values of  $p_{max}$  ( $D_f=2.9$ ).

According to the results shown in Figs. 2.3-6, the values of  $p_e$  and  $p_{max}$ , like  $D_f$ , influence not only the value of capillary pressure but also the shape of the curves.

The wetting phase relative permeability was calculated using Eq. 2.6 and the nonwetting phase relative permeability was calculated using Eq. 2.5 with different values of fractal dimension. The reason to do this was because Li and Horne (2002) reported that the Purcell model is the best fit to the experimental data of the wetting phase relative permeability for both drainage and imbibition processes but is not a good fit for the nonwetting phase. The results are plotted in Fig. 2.7. One can see that the relative permeability curves of the nonwetting phase are almost the same for different values of fractal dimension. However the relative permeability curves of the wetting phase are different for different values of fractal dimension. Fig. 2.7 shows that the wetting phase relative permeability curves with fractal dimension greater than 3.0 have different features from those with fractal dimension less than 3.0, as predicted by the model (see Eq. 2.6).

One can see that the values of the wetting phase relative permeability in the case where the fractal dimension over 3 are very small until the wetting phase saturation reaches about 80%. This phenomenon may be verified by future experimental data of relative permeability measured in The Geysers rock.

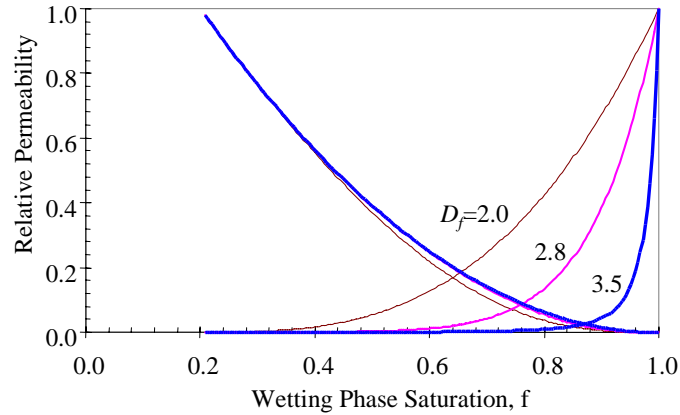


Figure 2.7: Typical relative permeability curves calculated using the new model with different values of fractal dimension.

Few experimental data of relative permeability in The Geysers rock or other type of rock with fractal dimension greater than 3.0 have been available in the literature. Therefore we cannot verify the new relative permeability models at present.

## **2.4 CONCLUSIONS**

Based on the present study, the following conclusions may be drawn:

1. Not only the heterogeneity but also the entry and maximum capillary pressure affects the shape of capillary pressure curves.
2. The effect of heterogeneity on the shape of wetting-phase relative permeability curves is significant. The greater the heterogeneity, the more curved the relative permeability curve.

### **3. FRACTURED ROCK RELATIVE PERMEABILITY**

This project is being conducted by Research Assistant Anson L. Villaluz, Senior Research Engineer Kewen Li and Prof. Roland N. Horne. The objective is to obtain measurements of steam-water relative permeability in real fractured rocks from geothermal reservoirs. This work is an extension of our earlier steam-water relative permeability studies which have mostly considered artificially uniform and high permeability rocks. Now that the relative permeability mechanisms have been understood, we are ready to embark on the more difficult measurements using heterogeneous, low permeability rocks from geothermal reservoirs.

#### **3.1 BACKGROUND**

Steam-water relative permeability and capillary pressure are important data for geothermal reservoir engineering. The Stanford Geothermal Program (SGP) has succeeded in making fundamental measurements of steam-water flow in porous media and made significant contribution to the industry. One of the important problems left to undertake is the measurement of steam-water relative permeability and capillary pressure in geothermal rock (most of the previous study was conducted in high permeability sandstone as a well-controlled test material.).

Using our existing steady-state CT method, we have measured steam-water relative permeability and capillary pressure in rock with permeability above 1 md ( $10^{-13}$  cm<sup>2</sup>). We were able to obtain the in-situ fluid saturation simultaneously using CT. For the geothermal rock with permeability smaller than 1 md ( $10^{-13}$  cm<sup>2</sup>), the steady-state CT method would work but it would take an extremely long time to conduct the experiments (weeks or even months). Hence the CT method is not practical to measure steam-water relative permeability in geothermal rocks.

To overcome this difficulty, we have embarked on different approach, by measuring the relative permeability curves in separate sections. We have concluded from our experimental data (Satic, 1998; Horne *et al.*, 2000; Mahiya, 1999; O'Connor, 2001; Li and Horne, 2000a) that steam-water relative permeability follows the Corey model and steam-water capillary pressure follow the Brooks-Corey model. We can measure the end-point steam-water relative permeability and saturation in the geothermal rock with permeability smaller than 1 md using our existing steady-state CT method or the direct weighing method developed by Li *et al.* (2001). Then the whole curve of steam-water relative permeability can be obtained using the Corey model and the capillary pressure curve can be obtained using the Brooks-Corey model. We plan to confirm the applicability of this approach first with nitrogen-water experiments, which are very much easier to conduct than the steam-water flows. This work was begun by Habana (2002), but ran into experimental difficulties.

The experimental study performed by Habana (2002) on a real fractured geothermal core showed results with pressure spikes occurring periodically during single-phase water injection. Erratic pressure spikes were observed during nitrogen-water relative permeability experiment in the same study. Some of the results are presented in Figures

3.1 and 3.2. The appearance of these transient effects indicated a difficulty with the experimental configuration, and prevented the measurement of relative permeability. In the continuation of this study, the apparatus has been redesigned and reconstructed to overcome these problems.

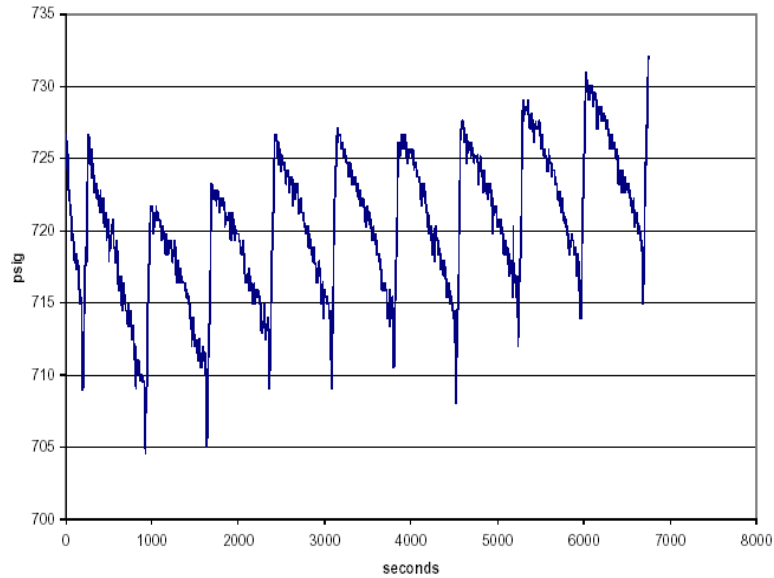


*Figure 3.1: Pressure at inlet during water injection. Constant water flow rate at 14 ml/min (Habana, 2002).*

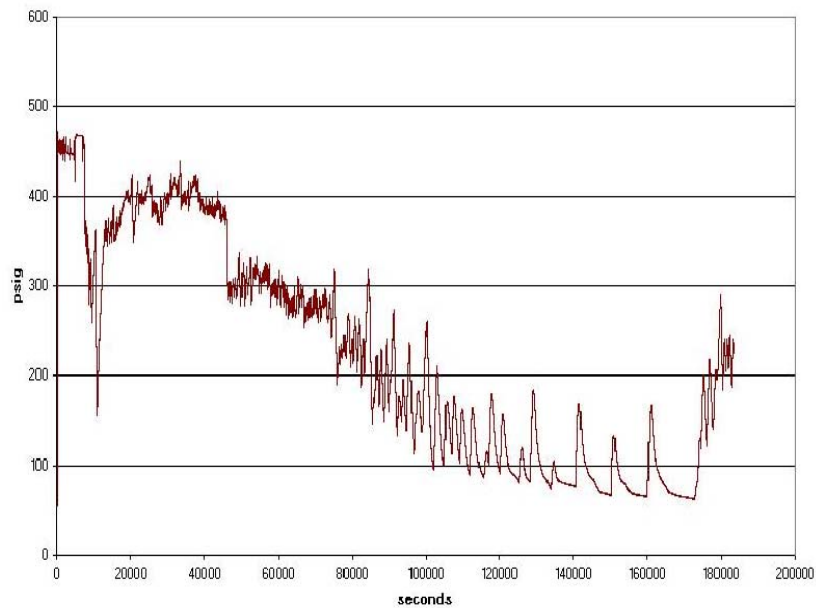


*Figure 3.2: Pressure at inlet for constant flow rate nitrogen-water experiment (Habana, 2002).*

### **3.2 EXPERIMENTAL METHODOLOGY**

The rock permeability will be measured using nitrogen gas at room temperature. Gas permeability is a function of pressure. Therefore, the flow measurements will be conducted at a series of different mean pressures and taking into account Klinkenberg slip effect.

A new core sample has been obtained from a depth of 2440.5m at The Geysers geothermal field. The core is 8.9 cm in length and 10.2 cm in diameter.

Nitrogen will be flowed into the core at different confining pressures. Confining pressure from 500 to 850 psig can be reached by injecting nitrogen around the heat shrink tubing inside the core holder. To apply higher confining pressure water can be used in place of nitrogen.

A schematic illustration of the experiment is shown in Figure 3.3.

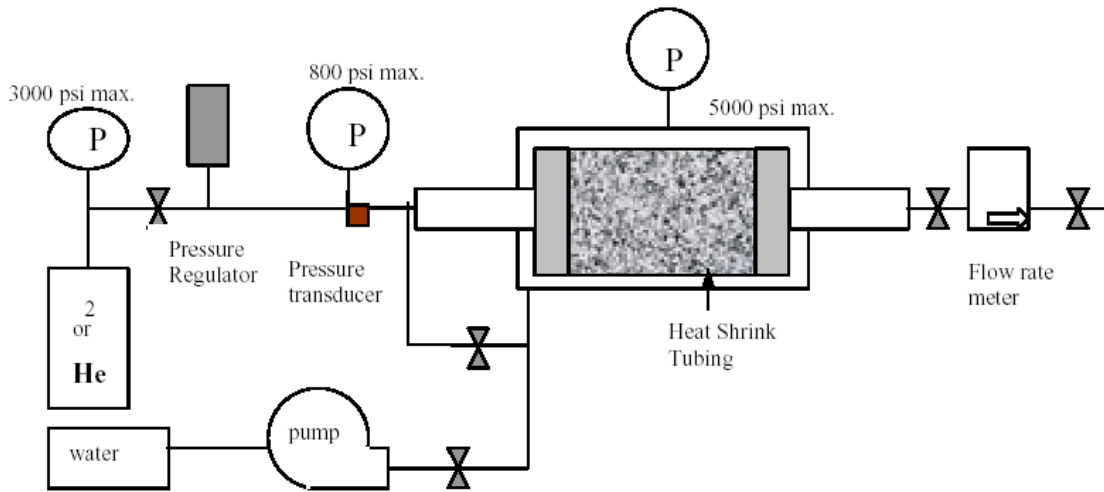


Figure 3.3: Schematic representation of apparatus

### **3.3 THEORETICAL BACKGROUND FOR ELECTRICAL RESISTIVITY**

As CT methods are less suitable for these low permeability experiments, we have been investigating electrical resistivity as a means of measuring water saturation. As a first step, electrical resistivity measurements were obtained to validate the relationship of resistivity with saturation via Archie's Equation.

This relationship can be represented by Equation 3.1:

$$I = bS_w^{-n} \quad (3.1)$$

where  $I = R_t/R_o$  is known as the resistivity index,  $R_t$  is the resistivity at a certain saturation,  $R_o$  is the resistivity at 100% water saturation,  $b$  is some function of tortuosity,

and  $n$  is the saturation exponent. Empirically,  $n=2$  for Berea sandstone from previous studies.

### 3.4 NITROGEN-WATER RELATIVE PERMEABILITY EXPERIMENTAL METHOD

As a preparation to doing relative permeability measurements in the geothermal core, and to have a deeper understanding of the experimentation process, an initial apparatus was configured to measure the data needed to calculate relative permeability.

The steady-state method for obtaining relative permeability data was employed. 1% NaCl solution and nitrogen gas were used as the two phases entering the core. A schematic diagram for the apparatus is presented in Figure 3.4. Electrical resistivity measurements were made simultaneously using an ordinary multimeter.

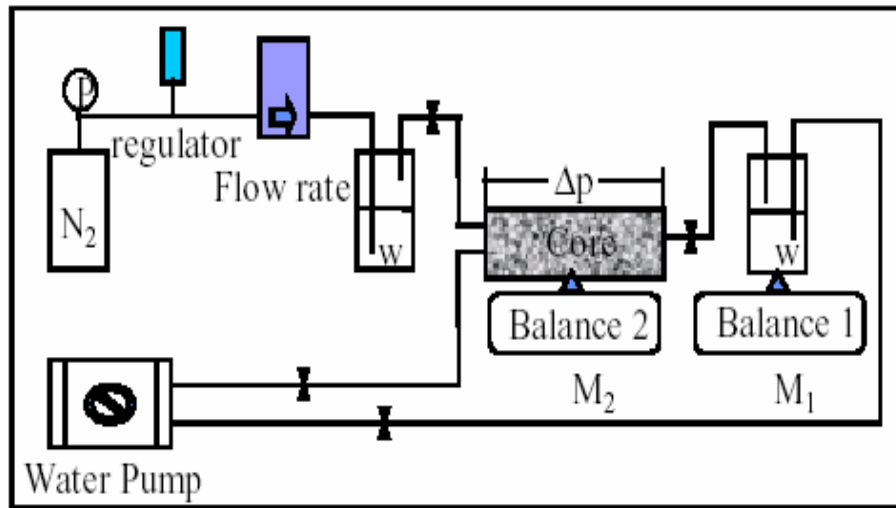


Figure 3.4: Schematic diagram of steady state  $N_2$ - $H_2O$  relative permeability test

In previous experiments, the core was put inside a rubber sleeve and two layers of shrink tubing were further placed atop to prevent leak, but after some time, leaks were again observed. This time, an aluminum core holder was used to be able to apply confining pressure and to eliminate leaks.

Saturation data were measured by weighing the core using Balance 2 as shown in Fig. 3.4 and verified using mass balance through Balance 1.

### 3.5 NITROGEN-WATER RELATIVE PERMEABILITY RESULTS IN BEREA SANDSTONE

Using Darcy's Law and assuming the ideal gas equation, effective permeability data were calculated at different saturation points.

As in a usual steady-state relative permeability measurement, saturation was altered by adjusting relative injectivity, which is basically the ratio between the flow rates of brine and nitrogen entering the system.

The results of the relative permeability experiment are presented in Figure 3.5.

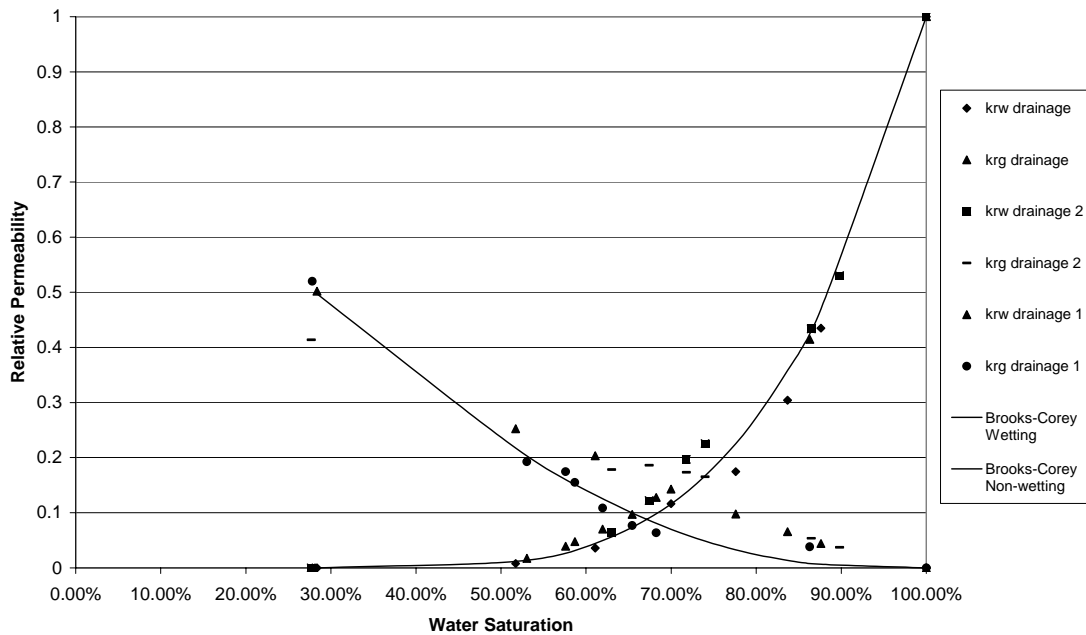


Figure 3.5. Nitrogen-Water Drainage Relative Permeability in Berea Sandstone

Figure 3.5 shows a summary of three drainage relative permeability experiments done with Nitrogen and 1% NaCl solution in Berea sandstone. To explain the legend, krw drainage, krg drainage, krw drainage 1 and krg drainage 1 were done with the improved core holder. Krw drainage 2 and krg drainage 2 were results presented on the April-June 2004 Quarterly Report (Fractured Rock Relative Permeability).

The general trend of the results seen in Figure 3.5 is acceptable. Relative permeability of a particular phase increases as saturation of that particular phase increases and vice versa. Plotted against a semiempirical model, the results can be observed generally to follow the Brooks-Corey model (with  $\lambda=2$ ).

Figure 3.6 summarizes the relative permeability measurements obtained during imbibition. Comparing Figure 3.5 with Figure 3.6, it can be seen that relative permeability of the nonwetting phase during imbibition is less than during the drainage process due to trapping

of the nonwetting phase. On the other hand, the effect of saturation history on the wetting phase relative permeability was observed to be minor, as expected. The results for  $k_{rw}$  imbibition 2 and  $k_{rg}$  imbibition 2 are not included in Figure 3.6 since that experiment suffered from leaks and therefore unreasonably low relative permeability values had been measured.

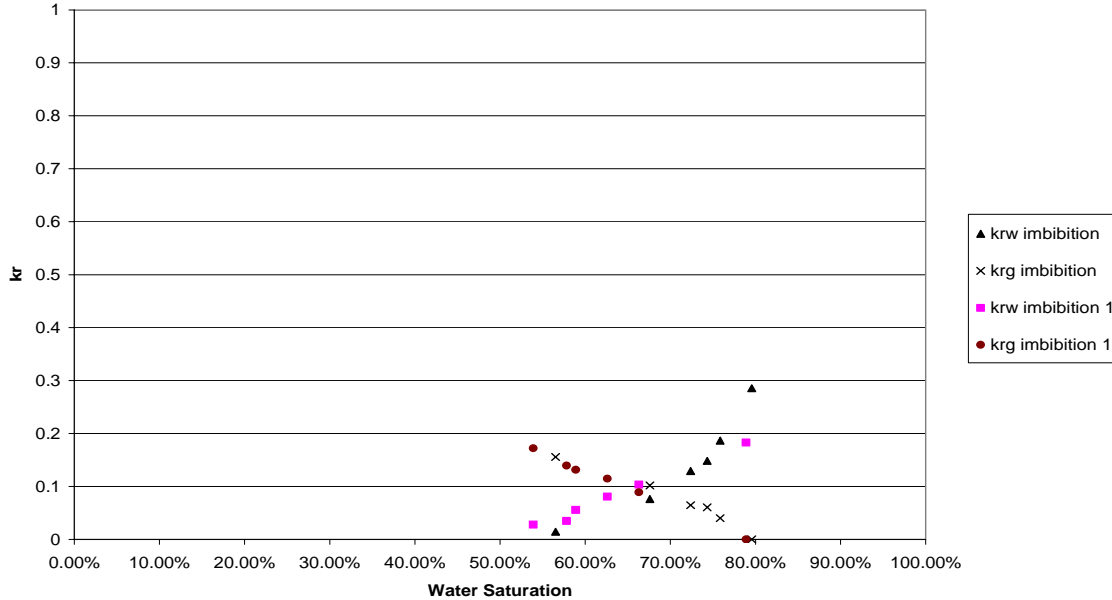


Figure 3.6. Nitrogen-Water Imbibition Relative Permeability in Berea Sandstone

### 3.6 RESULTS OF ELECTRICAL RESISTIVITY MEASUREMENTS DURING FLOW

The result of using Archie’s equation to correlate electrical resistivity with saturation while running the nitrogen-water relative permeability experiment is presented in Figure 3.7. An AC Meter was used for this purpose and the results seem to be better than those obtained using a DC measurement (April-June 2004 Quarterly Report Fractured Rock Relative Permeability). 100 Hz was chosen among the range of frequencies because it was found out that the phase shift of the current when applied to the system is least on this frequency. This usually gave the most accurate resistance readings in practice.

It can be observed from Figure 3.7 that Archie’s correlation seems to work well during both drainage and imbibition processes. One noteworthy observation is that the cementation factor appears to be higher (about 5.4) than that of usual Berea sandstones (about 2). This can be attributed to the firing of the sandstone core used in the experiment. During the firing process, clays (which are conductive materials) are calcified, therefore, decreasing the overall conductivity of the material and increasing its resistance/resistivity.

Another interesting observation from Figure 3.7 is that the resistivity indices are sensitive to the flow history, as the imbibition process indices are lower than those of the drainage process. This may be due to the fact that during drainage, the dominant "connected"

flowing fluid is gas which has relatively low conductivity while during imbibition, brine is the dominant "connected" flowing fluid.

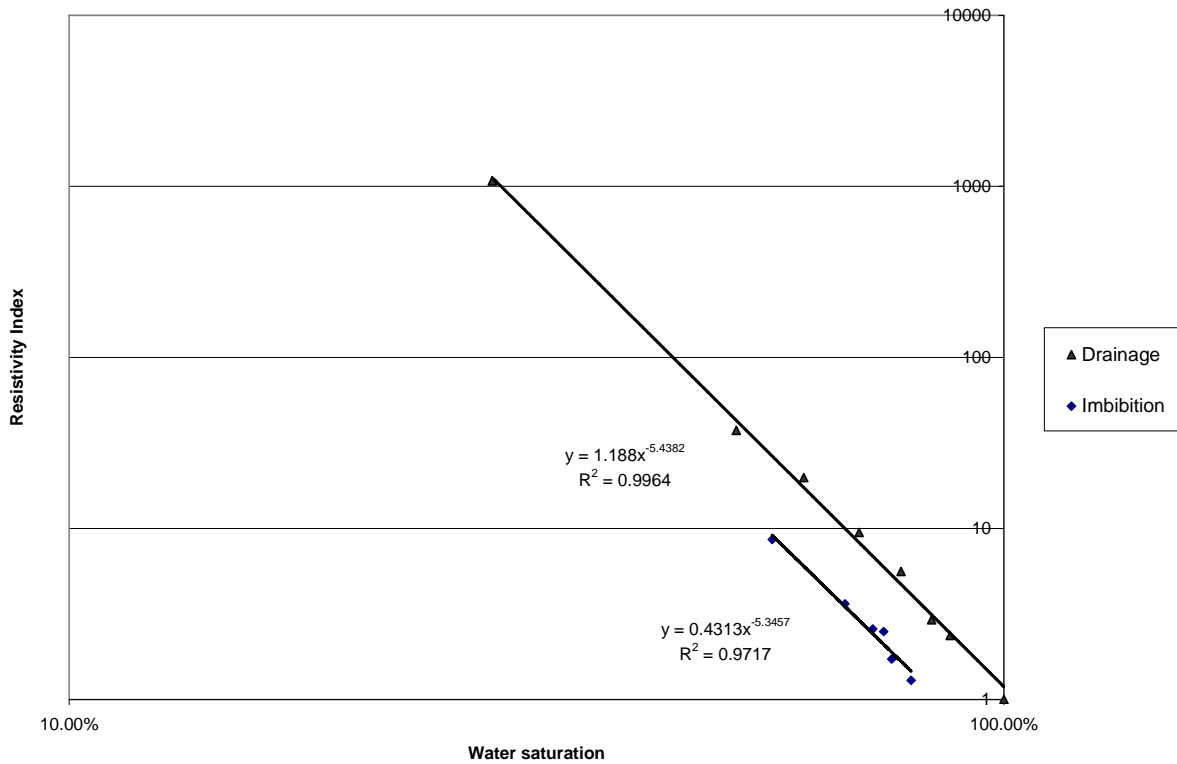


Figure 3.7. Archie's Correlation using 100 Hz AC Frequency

### **3.7 CONTINUING AND FUTURE WORK**

The next challenge will be relative permeability measurements of fractured rocks. A core holder that will be able to withstand higher pressures and hold a larger diameter core is being developed. The current flow system will be used for the experiments. Nitrogen-water as well as steam-water relative permeability will be measured.

Lastly, the application of pore network modeling with the aim of deriving relative permeability curves of fractured rocks will also be investigated to verify results from the fractured rock experiment.



#### **4. REFERENCES**

- Brooks, R.H. and Corey, A.T.: "Properties of Porous Media Affecting Fluid Flow," *J. Irrig. And Drain. Div.*, Proc. ASCE, IR2 (1966), Vol. 92, p. 61-88.
- Chen, C.-Y., Horne, R.N., and Fourar, M.: "Experimental Study of Liquid-Gas Flow Structure Effects on Relative Permeabilities in a Fracture," *Water Resources Research*, (Aug 2004a), Vol. 40, No.8, W08301.
- Chen, C.-Y., Li, K., and Horne, R.N.: "Experimental Study of Phase Transformation Effects on Relative Permeabilities in Fractures," paper SPE 90233, presented in SPE 2004 Annual Technical Conference and Exhibition, Houston, TX, USA, September.26-29, 2004b.
- Diomampo, G.P.: *Relative Permeability through Fractures*, MS thesis, Stanford University, Stanford, California (2001).
- Habana, M.D.: "Relative Permeability of Fractured Rock", MS report, Stanford University, Stanford, California, (2002).
- Horne, R.H., Satik, C., Mahiya, G., Li, K., Ambusso, W., Tovar, R., Wang, C., and Nassori, H.: "Steam-Water Relative Permeability," Proc. of the World Geothermal Congress 2000, Kyushu-Tohoku, Japan, May 28-June 10, 2000.
- Lomize, G.M.: *Flow in Fractured Rocks*, (Gosenergoizdat, Moscow, 1951).
- Li, K. and Horne, R.N. (2000a): "Steam-Water Capillary Pressure," SPE 63224, presented at the 2000 SPE Annual Technical Conference and Exhibition, Dallas, TX, USA, October 1-4, 2000.
- Li, K. and Horne, R.N.: "Fractal Characterization of The Geysers Rock," presented at the Geothermal Resource Council 2003 annual meeting, October 12-15, 2003, Morelia, Mexico; *GRC Trans.* **27** (2003).
- Li, K. and Horne, R.N.: "Universal Capillary Pressure and Relative Permeability Model from Fractal Characterization of Rock," presented at the 29<sup>th</sup> Stanford Geothermal Workshop on Geothermal Reservoir Engineering, Stanford University, Stanford, California, January 26-28, 2004.
- Li, K. and Horne, R.N.: "Experimental Verification of Methods to Calculate Relative Permeability Using Capillary Pressure Data," SPE 76757, Proceedings of the 2002 SPE Western Region Meeting/AAPG Pacific Section Joint Meeting held in Anchorage, Alaska, May 20-22, 2002.
- Li, K., Nassori, H., and Horne, R.N. (2001): "Experimental Study of Water Injection into Geothermal Reservoirs," to be presented at the GRC 2001 annual meeting, August 26-29, 2001, San Diego, USA; *GRC Trans.* V. **25**.
- Mahiya, G.: "Experimental Measurement of Steam-Water Relative Permeability," MS report, Stanford University, Stanford, California (1999).

- Meheust, Y., Schmittbuhl, J.: "Geometrical Heterogeneities and Permeability Anisotropy of Rough Fractures," *Journal of Geophysical Research*, (Feb. 2001); Vol.106, No.B2, p.2089-2102.
- Nicholl, M.J. and Glass, R.J.: "Wetting Phase Permeability in A Partially Saturated Horizontal Fracture," Proc. 5<sup>th</sup> Ann. Int. Conf. On High Level Rad. Waste Mgmt., 2007-19, American Nuclear Society, Las Vegas, Nevada, May 22-26,1994.
- Nicholl, M.J., Rajaram, H. and Glass, R.J.: "Factors Controlling Saturated Relative Permeability in a Partially Saturated Horizontal Fracture," *Geophysical Research Letters*, (Feb. 2000), Vol.27, No.3, p.393-396.
- O'Connor, P.A.: "Constant-Pressure Measurement of Steam-Water Relative Permeability," MS report, Stanford University, Stanford, California (2001).
- Pan, X., Wong, R.C. and Maini, B.B.: "Steady State Two-Phase Flow in a Smooth Parallel Fracture," presented at the 47<sup>th</sup> Annual Technical Meeting of the Petroleum Society in Calgary, Alberta, Canada, June 10-12, 1996.
- Persoff, P. and Pruess, K.: "Two-Phase Flow Visualization and Relative Permeability Measurement in Natural Rough-Walled Rock Fractures," *Water Resources Research* (May 1995) Vol. 31, No. 5, p. 1175-1186.
- Pruess, K. and Tsang, Y. W.: "On Two-Phase Relative Permeability and Capillary Pressure of Rough-Walled Rock Fractures," *Water Resources Research* (Sept. 1990) Vol. 26 No. 9, p. 1915-1926.
- Romm, E.S.: *Fluid Flow in Fractured Rocks*, "Nedra" Publishing House, Moscow (Translated from the Russian) (1966).
- Satik, C.: "A Measurement of Steam-Water Relative Permeability," Proceedings of 23<sup>rd</sup> Workshop on Geothermal Reservoir Engineering, Stanford University, Stanford, California (1998).
- Tokunaga, T.K. and Wan, J.M.: "Water Film Flow along Fracture Surfaces of Porous Rock," *Water Resources Research*, (Jun 1997), Vol.33, No.6, p.1287-1295.
- van Genuchten, M.T.: "A Closed Form Equation for Predicting the Hydraulic Conductivity of Unsaturated Soils," *Soil Science Society of America Journal*, (1980), Vol.44, No.5, p.892-898.
- Witherspoon, P.A., Wang, J.S.W., Iwai, K. and Gale, J.E.: "Validity of Cubic Law for Fluid Flow in a Deformable Rock Fracture," *Water Resources Research*, (1980), Vol. 16, No. 6, pp 1016-1024.
- Zimmerman, R.W. and Bodvarsson, G.S.: "Hydraulic Conductivity of Rock Fractures," *Transport in Porous Media*, (Apr 1996), Vol.23, No.1, p.1-30.